This document is confidential and is proprietary to the American Chemical Society and its authors. Do not copy or disclose without written permission. If you have received this item in error, notify the sender and delete all copies.

Low contact resistance on monolayer MoS2 field-effect transistors achieved by CMOS-compatible metal contacts

Journal:	ACS Nano		
Manuscript ID	nn-2024-07267z.R3		
Manuscript Type:	Article		
Date Submitted by the Author:	29-Jul-2024		
Complete List of Authors:	Sun, Zheng; Purdue University, ECE Kim, Seong Yeoul; The University of Texas at Dallas, Materials Science and Engineering Cai, Jun; Purdue University, electrical and computer engineering Shen, Jianan; Purdue University, Materials Engineering Lan, Hao-Yu; Purdue University, Elmore Family School of Electrical and Computer Engineering Tan, Yuanqiu; Purdue University School of Electrical and Computer Engineering; Purdue University Birck Nanotechnology Center Wang, Xinglu; The University of Texas at Dallas, Materials Science and Engineering Shen, Chao; Purdue University, School of Materials Engineering Wang, Haiyan; Purdue University, Materials Engineering Chen, Zhihong; Purdue University, ECE Wallace, Robert; University of Texas at Dallas, Depy. of Materials Science and ENgineering Appenzeller, Joerg; Purdue University, Electrical and Computer Engineering		

SCHOLARONE™ Manuscripts

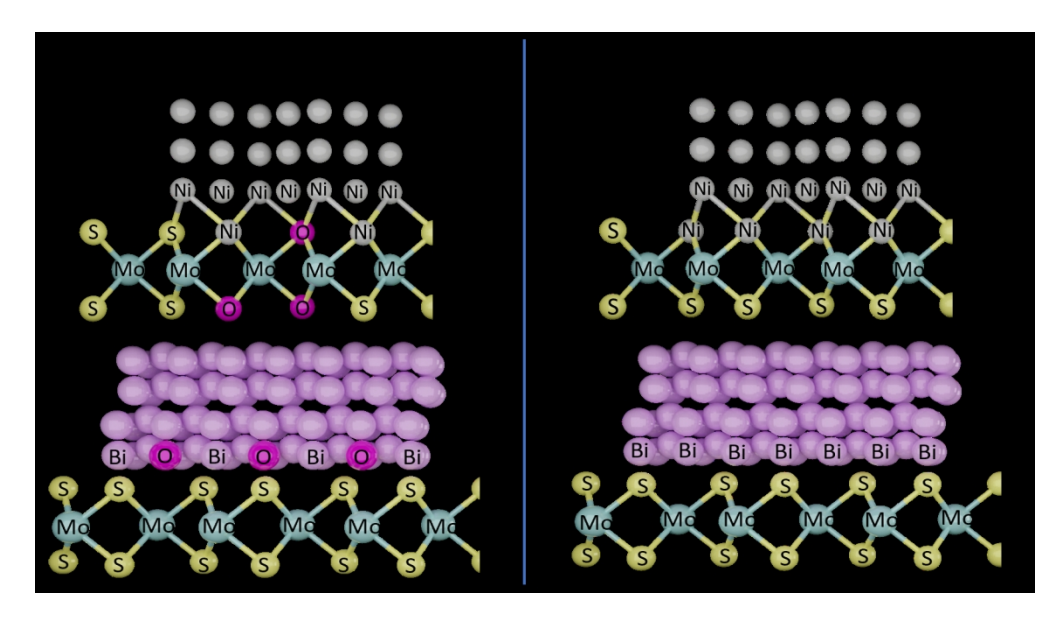


Table of Contents

137x77mm (330 x 330 DPI)

Low contact resistance on monolayer MoS₂ fieldeffect transistors achieved by CMOS-compatible metal contacts

Zheng Sun^{1,2†*}, Seong Yeoul Kim³[†], Jun Cai^{1,2}, Jianan Shen[‡], Hao-Yu Lan^{1,2}, Yuanqiu Tan^{1,2}, Xinglu Wang³, Chao Shen[‡], Haiyan Wang^{1,‡}, Zhihong Chen^{1,2}, Robert M. Wallace³, Joerg Appenzeller^{1,2}

¹School of Electrical and Computer Engineering, Purdue University, West Lafayette, Indiana 47907, United States; ²Birck Nanotechnology Center, Purdue University, West Lafayette, Indiana 47907, United States; ³Department of Materials Science and Engineering, University of Texas at Dallas, Richardson, Texas 75080, United States; ⁴School of Materials Engineering, Purdue University, West Lafayette, Indiana 47907, United States;

†These authors contributed equally: Zheng Sun, Seong Yeoul Kim.

*sun996@purdue.edu

Abstract

Contact engineering on monolayer layer (ML) semiconducting transition metal dichalcogenides (TMDs) is considered the most challenging problem towards using these materials as a transistor

channel in future advanced technology nodes. The typically observed strong Femi level pinning induced in part by the reaction of the source/drain contact metal and the ML TMD frequently results in a large Schottky barrier height, which limits the electrical performance of ML TMD field-effect transistors (FETs). However, at a microscopic level, little is known about how interface defects or reaction sites impact the electrical performance of ML TMD FETs. In this work, we have performed statistically meaningful electrical measurements on at least 120 FETs combined with careful surface analysis to unveil contact resistance dependencies on the interface chemistry. In particular, we achieved a low contact resistance for ML MoS₂ FETs with ultra-high vacuum (UHV, 3×10⁻¹¹ mbar) deposited Ni contacts, ~500 ohm·μm, which is 5 times lower than the contact resistance achieved when deposited at high vacuum (HV, 3×10⁻⁶ mbar) conditions. These electrical results strongly correlate with our surface analysis observations. X-ray photoelectron spectroscopy (XPS) revealed significant bonding species between Ni and MoS2 under UHV conditions compared to HV. We also studied the Bi/MoS₂ interface under UHV and HV deposition conditions. Different from the case of Ni, we do not observe a difference in contact resistance or interface chemistry between contacts deposited under UHV and HV. Finally, this article also explores the thermal stability and reliability of the two contact metals employed here.

Keywords:

Contact interface engineering, low contact resistance, monolayer MoS₂, field-effect transistors, CMOS-compatible, thermal stability, interface chemistry

Main Text

Monolayer (ML) semiconducting transition metal dichalcogenides (TMDs), including ML MoS₂, ML WSe₂ and ML WS₂, are considered by leading semiconductor companies¹⁻³ as potential channel materials in field-effect transistors (FETs) for future advanced technology nodes. The atomically thin body of ML TMDs with ideally no dangling bonds allows for extreme channel length scaling without introduction of significant short channel effects⁴. In the past ten years, the main challenge for the development of high-performance ML TMD FETs has been a too high contact resistance between the source/drain metals and the semiconducting channel materials⁵. To overcome this challenge, different metals, such as Ni, Sc, Ti, Au, Sn^{4–7}, were employed to lower the contact resistance. Strong Fermi-level pinning induced by metal-induced gap states (MIGS) is found to be the key reason causing the high contact resistance⁵. Recent advancements have highlighted that contact engineering is a critical approach to mitigating high contact resistances, particularly by employing Sb and Y contacts^{8,9}. The optimization of the deposition process markedly influences the chemical reactions and the resulting compounds formed at the metal-TMD interface. interface. According to the Schottky-Mott rule, the Schottky barrier height (SBH) at the source/drain-to-channel interface should scale with the metal work function, resulting in smaller barriers for electron injection into the conduction band for low work function metals. However, experimentally, the SBH is rather insensitive to the work function of many metals used as contacts to MoS₂. This is especially true for some evaporated metal contacts, such as Ti, Cu, $Cr^{5,10,11}$. Several reports observed, e.g. by X-ray photoelectron spectroscopy (XPS)^{12–15}, that the metal deposition can result in a chemical reaction at the metal-to-channel interface that can be expected to impact – in a positive or negative fashion – the contact quality and is referred to in the following as "covalent type" of metal contact. However, there is only circumstantial evidence about how the surface chemical reaction relates to the contact resistance^{6,16–18}, and therefore a statistical assessment of the electrical performance that correlates the contact resistance with the

microscopic interface properties is missing at this point in time. In addition, there is another class of metals, such as Bi, Sb, In, Ag, Au^{8,12,19,20}, that are believed to not react with the 2D channel upon deposition, which will be referred to in the following as "van der Waals (vdW) type" contacts. vdW type contacts are characterized by an atomically thin vdW gap between the metal and the TMD that acts as a tunneling barrier for carrier injection. It is believed that in particular semimetals such as Bi and Sb used as contacts to TMD channels benefit from a reduced Fermilevel pinning, resulting in lower SBHs¹⁹ and better contacts.

Here we present a comprehensive study that uses two metals – Ni as an example of a covalent type of contact and Bi as vdW type of contact – deposited under two different vacuum conditions to correlate the surface chemistry occurring at the metal-to-channel interface with a statistically relevant set of electrical data. Note in particular that there exists no study that evaluates the vacuum impact in case of vdW type contacts to the best of our knowledge. As discussed in detail below, we have achieved low contact resistance values of around 500 to 600 ohm um in ML MoS₂ FETs by utilizing ultrahigh vacuum (UHV) metal deposition for Ni contact. This is a record low contact resistance for covalent type of Ni contacts. Moreover, we found characteristic features in the surface analyses we performed that corroborate that a more pronounced reaction between Ni and MoS₂ in case of Ni deposited under UHV conditions correlates with this low contact resistance value, i.e. a stronger interaction between Ni and MoS₂ under UHV. We also found that the contact resistance in case of Bi-contacted ML MoS₂ does not show a clear correlation with the vacuum conditions during deposition. Our XPS analysis reveals that there is no detectable chemical reaction between Bi and ML MoS₂ under UHV or HV deposition, consistent with the statement that Bi acts as a vdW type contact.

Furthermore, we have studied the thermal stability of our two different contact types. This is important, since back-end-of line compatible processes require a thermal budget that does not exceed 400°C and understanding the response of contacts to TMDs at elevated temperatures is critical to evaluate their usefulness for future transistor technologies. In case of Ni, we observe an increase in contact resistance after annealing at 100°C without a change of the XPS spectrum in this temperature range. We speculate that diffusion of Ni into the channel area and oxidation of this diffused Ni could be responsible for our observations, following the arguments presented in a previous publication²¹. For the encapsulated Bi contacts, the contact resistance is not impacted by the post annealing process. It is noteworthy that this observation is rather different from a previous report²². In our case, XPS reveals that Bi does not react with MoS₂ up to 400°C, and since we prevented Bi evaporation through capping our contacts with Au, we did consequently not observe a degradation of contact resistance even for an annealing temperature above the melting point of Bi.

Results and Discussion

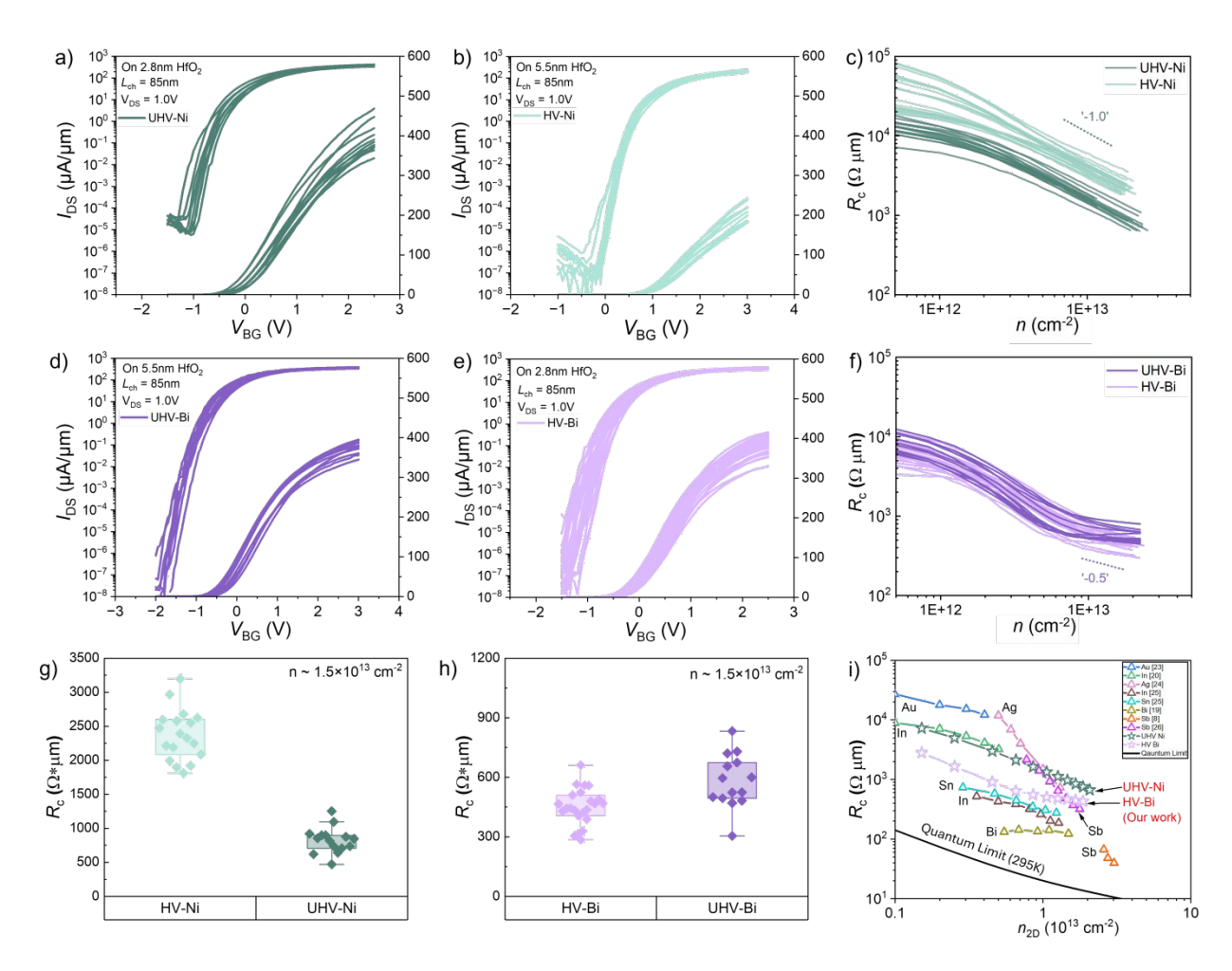


Figure 1. Transfer characteristics of UHV/HV-Ni contacted ML MoS₂ FETs and UHV/HV-Bi contacted ML MoS₂ FETs a. Transfer curves of UHV-Ni contacted ML MoS₂ FETs with $L_{CH} \sim 85$ nm in logarithmic (left) and linear (right) scale. **b.** Transfer curves of HV-Ni contacted ML MoS₂ FETs with $L_{CH} \sim 85$ nm. **c.** Contact resistance of UHV/HV-Ni contacted ML MoS₂ FETs versus carrier density. **d.** Transfer curves of UHV-Bi contacted ML MoS₂ FETs with $L_{CH} \sim 85$ nm. **e.** Transfer curves of HV-Bi contacted ML MoS₂ FETs with $L_{CH} \sim 85$ nm. **f.** Contact resistance of UHV/HV-Bi contacted ML MoS₂ FETs versus carrier density. **g.** Contact resistance comparison between HV-Ni and UHV-Ni contacted ML MoS₂ FETs at a carrier density of 1.5×10^{13} cm⁻². **h.** Contact resistance comparison between HV-Bi and UHV-Bi contacted ML MoS₂ FETs at a carrier density of 1.5×10^{13} cm⁻². **h.** Contact resistance of a selected set of ML MoS₂ FETs^{8,19,20,23-26}

To statistically evaluate the overall electrical performance, 60 UHV-Ni and 64 HV-Ni contacted ML MoS₂ FETs were fabricated. UHV Ni is deposited at 3×10⁻¹¹ mbar and HV-Ni is deposited at 3×10⁻⁶ mbar. Transfer characteristics of UHV-Ni and HV-Ni contacted ML MoS₂ FETs are shown in Figure 1a) and 1b). Good on-current levels and off-state behavior are observed for both UHV-Ni contacted and HV-Ni contacted MoS₂ FETs. Note that the current level of UHV-Ni devices can achieve up to 470 μ A/um for the best device at $V_{DS}=1$ V, $V_{GS}=2.5$ V. To extract the contact resistance, four different channel length FETs were fabricated (85nm, 185nm, 385nm and 985nm). A clear channel length dependent behavior is observed for both UHV-Ni and HV-Ni contacted FETs, as shown in the Supplementary Figure. S1a) and b). The contact resistance is extracted employing the transfer length method (TLM). Figure 1c) shows the contact resistance versus carrier density for UHV-Ni contacted and HV-Ni contacted ML MoS₂ FETs. At the same carrier density, the average contact resistance of UHV-Ni is substantially lower than the average contact resistance of HV-Ni contacted FET. Note that one may argue that the use of different HfO₂ thicknesses for UHV and HV deposited devices will impact the Schottky barrier thickness λ at the source/drain to channel interfaces, and the higher contact resistance in case of HV-Ni devices is just a result of this.²⁷ However, since the carrier density is extracted considering a combination of oxide capacitance and the air gap between ML MoS₂ and the dielectric layer²⁸, the capacitance equivalent thicknesses (CET) of HV-Ni FETs and UHV-Ni FETs are 2.2nm and 2.09nm, respectively, which are very similar values. This implies that λ is almost the same for both cases, and that the impact of a change of λ is not likely responsible for the experimental observation.²⁹ At the same time, as expected, the sheet resistance does not depend on the vacuum pressure for deposition, as shown in Supplementary Figure S2b). All devices show the expected $d(\log(R_C))/d(\log(n))$ slope of about -1 that is reflecting the response of the source/drain Schottky barriers to the applied gate field underneath the metal contact areas in our back-gated devices³⁰.

Figure 1g) summarizes the difference in contact resistance values of UHV-Ni and HV-Ni contacted ML MoS₂ at a carrier density of 1.5×10¹³ cm⁻². The lowest experimentally determined contact resistance in case of UHV-Ni FETs is ~500 ohm·µm. The average contact resistance of UHV-Ni FETs is about 5 times lower than for HV-Ni FETs due to the reaction of Ni with MoS₂, as discussed in greater detail below. The contact resistance of UHV-Ni contacted ML MoS₂ FETs is benchmarked against other published results^{8,19,20,23–26,31,32} in Figure 1i). Except for the Ni contacts employed in this work that were deposited under UHV conditions, all other metal contacts shown in the graph fall into the vdW type contact category, highlighting that competitive contacts can be achieved with covalent type metals if deposited under the right conditions through interface engineering. Output characteristics are shown for all four metal contact cases in Supplementary Figure S3c) and d). All output characteristics show good current saturation of our "well-tempered" devices. The lower current level in case of HV-Ni is apparent in figure S3c). The off-state behavior is shown in Supplementary Figure S4, S5. Both UHV-Ni and HV-Ni contacted FETs present good inverse subthreshold slopes, 60~80 mV/dec for UHV-Ni and 70~90 mV/dec for HV-Ni, respectively.

Different from the case of Ni, the contact resistance for MoS₂ FETs contacted with Bi was found to be independent of the vacuum deposition conditions. Bismuth contacts have been demonstrated with very low contact resistance on ML MoS₂ FET before, and the results have been interpreted as a consequence of metal induced gap states (MIGS) resulting in a favorable line-up of the semimetal Fermi level to the conduction band of the TMD^{8,19}. The results presented here expand on the existing literature in presenting a statistically relevant number of devices, i.e. in total more than 150 Bi-contacted FETs, while exploring the impact of the vacuum conditions on the contact quality. UHV-Bi and HV-Bi contacts are deposited under vacuum at 3×10⁻¹¹ mbar (UHV) and

3×10⁻⁶ mbar (HV) respectively. 40 UHV-Bi contacted and 112 HV-Bi contacted MoS₂ FETs were fabricated with four different channel lengths, showing very reproducible behavior as evident from Figure 1d) and 1e), 1f) and 1h. High on-current levels (around 400 µA/µm) are achieved for the shortest devices (85nm) explored here, and good on/off current ratios ($\sim 10^8$) are apparent from the figures. A clear channel length dependence is observed for both UHV-Bi and HV-Bi contacted FETs, as shown in the Supplementary Figures S1c) and d). The extracted contact resistance versus carrier density for UHV-Bi and HV-Bi is shown in Figure 1f). The fact that in this case the UHV-Bi and HV-Bi devices exhibit an extremely similar behavior further supports our statement from above about CET being comparable for the two different HfO₂ thicknesses employed. Different from the case of Ni-contacted devices, Bi-contacted FETs show a change of slope from $d(\log(R_C))/d(\log(n))=-1$ to -0.5 for the highest carrier concentrations. While a slope of -0.5 may hint at having reached the quantum limited contact resistance, $R_{c,min}$ = $h/(2q^2)$ sqrt $(\pi/2n_{2D})$, 8 the actual resistance value above 10^{13} cm⁻² is not consistent with the expected value of 20 ohm·µm, likely because of the existence of a vdW gap between Bi and the TMD, as mentioned in a previous publication¹⁹. This gap will add another carrier concentration independent resistance in series to the predicted quantum limit, but would not mask the -0.5 slope. Figure 1h) illustrates all contact resistance values extracted for UHV-Bi and HV-Bi contacts at a carrier density of 1.5×10¹³ cm⁻². Noteworthily, the average contact resistance of UHV-Bi devices is slightly higher than the average contact resistance for HV-Bi, which may be related to a somewhat different vdW tunneling barrier for these two cases¹⁹. Exemplary output characteristics are shown in Supplementary Figure S3a) and S3b), which show a similar behavior as UHV-Ni with good current saturation at higher drain voltages. Supplementary Figure S4a) and S4b) summarize the off-state behavior for all Bi-contacted devices. Interestingly, significantly higher SS-values are observed for both UHV-Bi and HV-Bi contacts at L_{ch} =85nm if compared to

the Ni-contacted devices. This is accompanied by a more negative threshold voltage, as shown in Supplementary Figure S4b). At this stage, we speculate that charge transfer doping from the Bi contacts may have impacted the device off-state.¹⁹

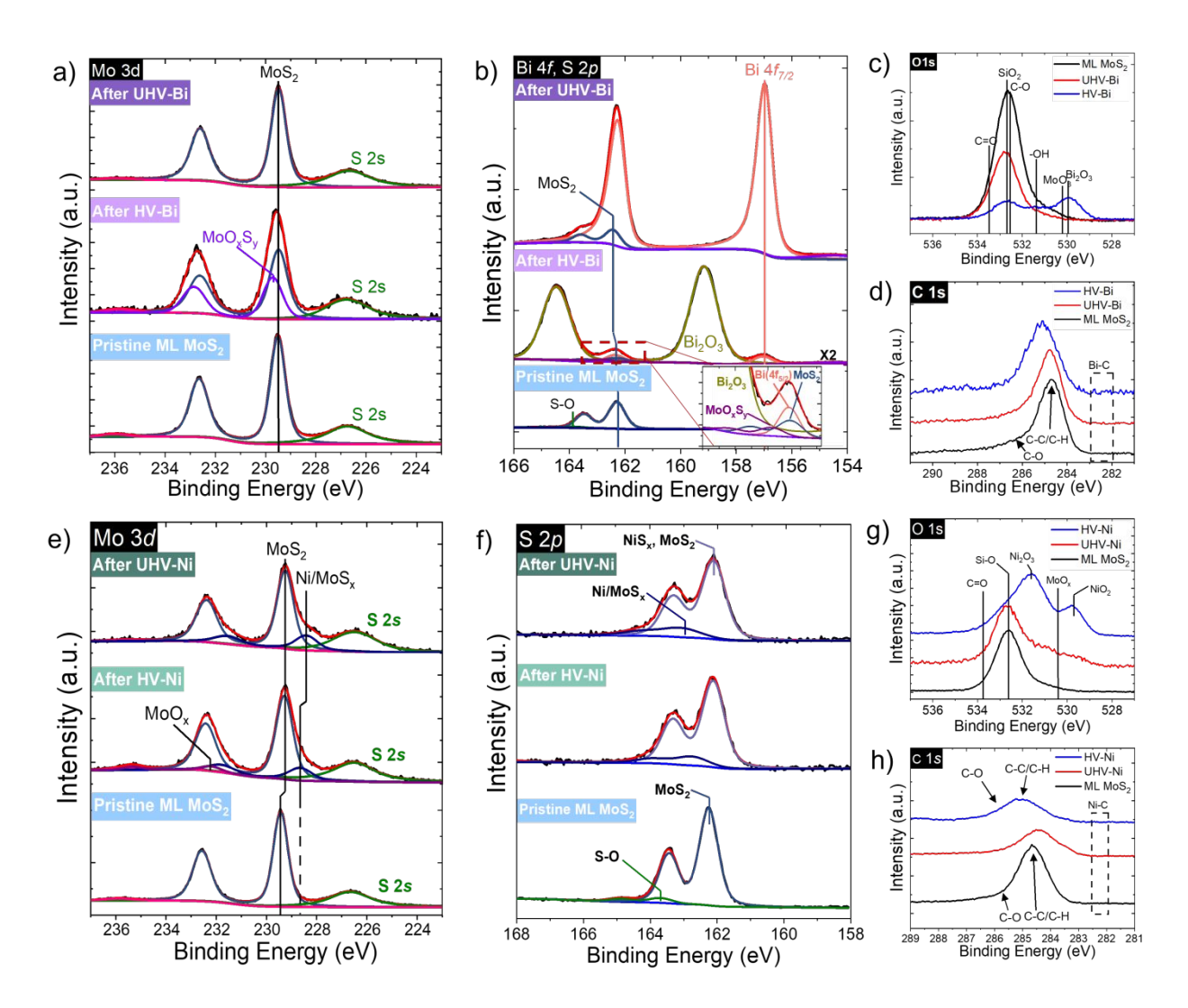


Figure 2. Interface study of Bi-MoS₂ and Ni-MoS₂ for different contact metal deposition conditions. XPS spectra for **a.** Mo 3d, **b.** Bi 4f and S 2p, **c.** O 1s, and **d.** C 1s core levels of MoS₂ samples before and after Bi deposition under UHV and HV conditions. XPS spectra for **e.** Mo 3d, **f.** S 2p, **g.** O 1s and **h.** C 1s core levels of MoS₂ samples before and after Ni deposition under UHV and HV conditions.

Multiple publications have explored the impact of the ambient conditions during metal deposition as well as the impact of various fabrication process steps.^{6,13,33,34} Correlating the metal deposition conditions with the contact resistance has also been reported⁶. However, there exists no statistical electrical measurement and corresponding surface analysis that explains the contact resistance in the context of the microscopic details at the source/drain metal contact to TMD interface.

ML MoS₂ is grown by CVD on SiO₂ substrates, and samples were loaded into an ultrahigh vacuum (UHV) cluster system to investigate the properties of the various metal-to-MoS₂ interfaces. High-resolution XPS is employed before metal deposition to characterize the pristine MoS₂. Next, the sample is transferred through a transfer tube ($<3\times10^{-11}$ mbar) to the e-beam UHV evaporation chamber ($<3\times10^{-11}$ mbar) for Bi and Ni deposition and XPS is used again to characterize the interface. For the HV-deposited metals, the sample was removed after initial inspection of the MoS₂ from the UHV cluster and transferred to the HV e-beam deposition system ($<1\times10^{-6}$ mbar), minimizing the ex-situ transfer time to about 5 minutes in every run. Another XPS inspection is performed in the UHV cluster system after HV deposition.

Figure 2 shows the surface and interface characteristics of XPS spectra before and after metal deposition under HV or UHV ambient with no capping layer. In case of Bi deposited on MoS₂, no significant reaction products with the MoS₂ are visible for UHV-Bi and HV-Bi as reported in literature using other metals. ^{12,13,15,17,18} In particular, the O *Is* and C *Is* spectra display no detectable reaction features at the contact interface, as evident from Figure 2c) and d). However, the detection of Bi-oxide, likely Bi₂O₃, for the HV Bi deposition is evident, as noted in Figures 2 b) and c). In contrast, the detection of Bi-oxide for the UHV deposition process is below the detection limit. This result indicates that oxygen sources in the HV chamber, such as water or -

OH residual, as well as subsequent air-exposure due to the ex-situ transferring process, participate in the reaction during the Bi deposition process and can result in Bi-oxide formation.

To further evaluate the surface and interface characteristics, curve fitting for Mo 3d, S 2p, and Bi 4f spectra was performed using AAnalyzer³⁶ to extract the information details provided in Table 1. The peak labeled MoS₂ in Figure 2(a) shows a consistent full width at half-maximum (FWHM) of 0.68 eV before and after UHV-Bi deposition, indicating no detectable interfacial reaction occurred in this case. These results are consistent with the thermodynamic prediction of unfavorable interfacial reaction products, that $\Delta G^{\circ}_{f,MoS_2}$ (-112.95 kJ/mol) is lower than $\Delta G^{\circ}_{f,Bi_2S_3}$ (-46.87 kJ/mol). However, in the HV-Bi sample, Mo 3d clearly shows two features of MoS₂ at 229.46 eV (MoS₂), and another feature appeared at 229.72 eV (MoO_xS_y). It is plausible that the feature observed at higher binding energy is MoO_xS_y, which is a result of the ex-situ transferring process and oxygen sources in the HV chamber, such as water or -OH residuals.

To complement these findings, atomic force microscopy (AFM) was also performed, with the results displayed in Figure 4c). From the before annealing sample (Figure 4c)), we conclude that Bi follows the Volmer-Weber growth model, causing islands formation on MoS₂. The exposed MoS₂ surfaces between islands could result in oxidation. However, the oxidation products detected for thin (photoelectron transparent) Bi layers (thickness < 2nm) do not impact the device performance, since more than 20 nm of Bi is deposited for all devices to be clustered together, followed by the deposition of an Au capping layer in the same HV e-beam evaporator.

Following the characterization approach, we employed for Bi, the Ni-to-MoS₂ contact interface was carefully characterized before and after metal deposition under HV and UHV conditions.

Previously, some of us reported by employing Raman and XPS, a reaction between Ni and MoS₂

(bulk and bilayer). 15 Here we are reporting data on monolayer MoS₂. Figure 2e) shows that Mo 3d exhibits a shoulder at lower binding energies (BEs), which indicates the presence of MoS_x reaction products after Ni deposition, irrespective of the vacuum conditions. Using careful curve fitting, we identified the BE of Ni/MoS_x to be 228.66 eV for HV and 228.40 eV for UHV deposition conditions, respectively. The BE difference could occur due to the metallic properties of the Ni/MoS_x bonding species, where it is noted that the Ni/MoS_x feature in the UHV-Ni sample has more metallic properties. The HV-Ni sample has a lower Ni/MoS_x relative intensity $(I_{\text{Ni/MoSx}}/I_{\text{Mo3d total}})$ than the UHV-Ni sample, i.e. the intensity is 17% of the Mo 3d core level peak for the HV-Ni sample and 20% for the UHV-Ni sample, respectively. Oxidation of MoS₂ under high vacuum deposition conditions of Ni, i.e. a MoO₃ feature, can be observed at 232.18 eV. This result indicates that oxygen in the HV chamber, such as water or -OH residuals, participate in the reaction during the deposition process. Because MoO₃ ($\Delta G^{\circ}_{f,MoO_3}$ =-266.67 kJ/mol) is thermodynamically more stable than MoS₂ ($\Delta G^{\circ}_{f,MoS_2} = -112.95 \text{ kJ/mol}$), NiS ($\Delta G^{\circ}_{f,NiS} = -79.5$ kJ/mol) and Ni₂O₃ ($\Delta G^{\circ}_{f,Ni_2O_3}$ = -163.17 kJ/mol), it is plausible that MoO₃ is the remaining reaction product. Figure 2g) shows that Ni-oxide formation is detected in the HV-Ni sample due to the ex-situ transferring process and the existence of oxygen sources, such as water and -OH residuals. As a result of the existence of oxygen sources, the HV deposition condition forms fewer bonding species with the MoS₂, as observed by a lower Ni/MoS_x intensity in Figure 2e). The lower Ni/MoS_x intensity shown in Figure 2e) in case of HV-Ni if compared to UHV-Ni, results from the forming bonding of MoS₂ with oxygen, making it unavailable for the bonding species with Ni. Consistent with this observation, a stronger Ni/MoS_x feature is visible in the S 2p spectra for UHV-Ni in Figure 2f) if compared to HV-Ni. We also conclude that the noticeably wider FWHM of 0.82 eV (0.78 eV) at a binding energy of 162.12 eV (162.13 eV) in the UHV (HV) sample compared to the reference sample before Ni deposition, is a consequence of Nickel

reacting with Sulfur, forming NiS_x . NiS_x formation is likely due to out-diffused Sulfur, consistent with the increase in the S 2s peak intensity (Figure 2e).

For the devices, the Ni contact layer was 50 nm thick. With minimal spurious oxidation detected for deposition under UHV conditions (Figure 2g)), the significant Ni-oxidation detected for HV samples may be responsible for the higher contact resistance extracted from the electrical characterization of the 64 HV-Ni FETs relative to the 60 UHV-Ni FETs (Figure 1g)). It is noteworthy that the Ni and Ni-silicide electrical properties have been reported as sensitive to impurities such as oxygen. ^{37,38} In 2-dimensional semiconductor transistors, The device measurements, and the interface characterizations prove that the quality of the contact interface and electrical properties are significantly affected by the metallization ambient, that is, the Ni-MoS₂ contact interface reported to have a stronger bonding, i.e., covalent-like contact.

Table 1 FWHM and the binding energy corresponding to the MoS₂ feature of the Mo $3d_{5/2}$ and S $2p_{3/2}$ spectra before and after Bi(Ni) deposition under UHV and HV conditions and subsequent air exposure of the ex-situ transferring process

RE (FWHM)

Metals	Substrates	Core Level	Before (eV)	UHV (eV)	HV (eV)
Bi (van der Waals)	MoS_2	Mo 3d _{5/2}	MoS ₂ : 229.45 (0.70)	MoS ₂ : 229.41 (0.69)	MoS ₂ : 229.46 (0.81) MoO _x S _y : 229.72 (0.91)
		S $2p_{3/2}$	MoS ₂ : 162.29 (0.69)	MoS ₂ : 162.27 (0.68)	MoS ₂ : 162.51 (0.84) MoO _x S _y : 54.41 (0.85)
Ni (Covalent)	MoS ₂	Mo 3d _{5/2}	MoS ₂ : 229.42 (0.67)	MoS ₂ : 229.23 (0.76) Ni/MoS _x : 228.40 (1.02)	MoS ₂ : 229.28 (0.78) Ni/MoS _x : 228.66 (1.10) MoO ₃ : 232.18 (0.92)
		$S 2p_{3/2}$	MoS ₂ : 162.24 (0.67)	NiS,MoS ₂ : 162.12 (0.82) Ni/MoS _x : 163.07 (1.09)	NiS,MoS ₂ : 162.13 (0.78) Ni/MoS _x : 162.56 (1.05))

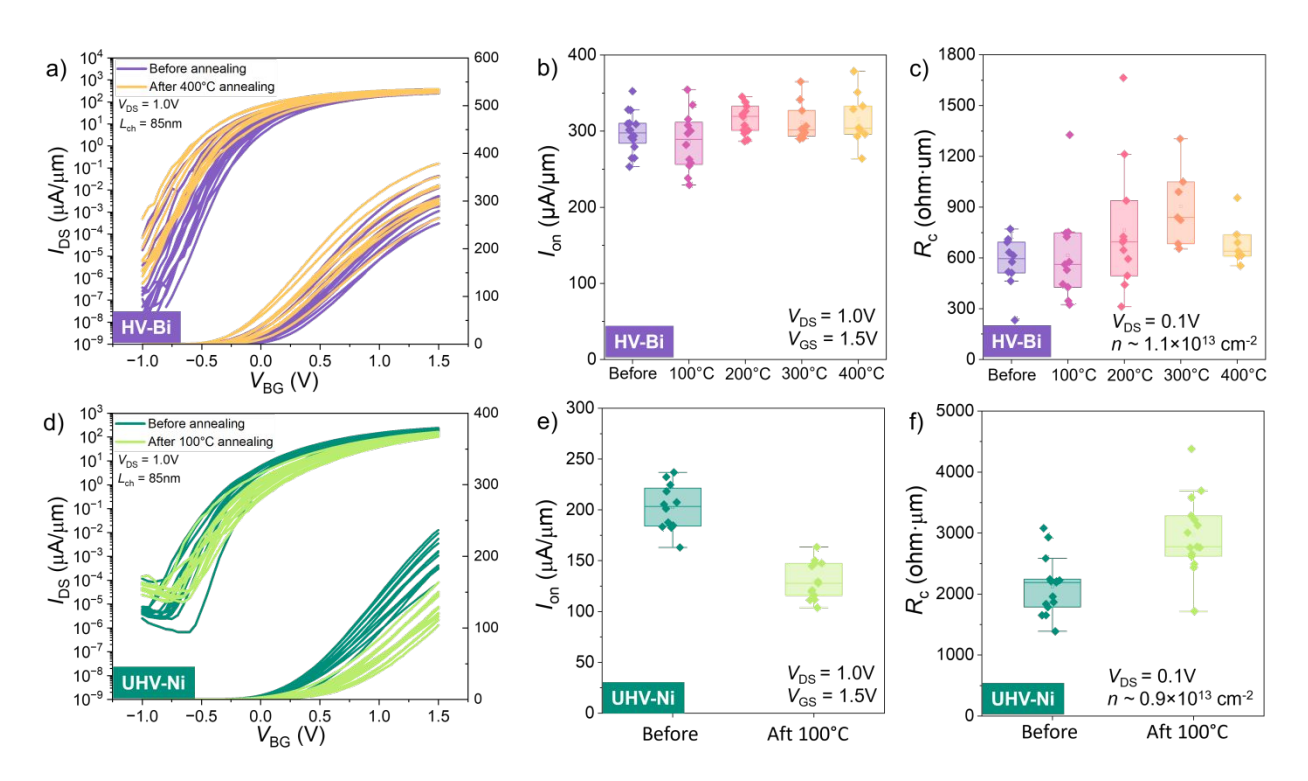


Figure 3. Thermal reliability study of UHV-Ni contacted and HV-Bi contacted ML MoS₂

FETs. a). Transfer curves of HV-Bi contacted ML MoS₂ FETs with $L_{\rm CH} \sim 85$ nm before and after various annealing process steps. b). $I_{\rm on}$ of HV-Bi contacted ML MoS₂ FETs at $V_{\rm GS} = 1.5$ V before and after annealing at different temperatures. c). Contact resistance of HV-Bi contacted MoS₂ FETs $n \sim 1.1 \times 10^{13}$ cm⁻² before and after annealing at different temperatures. d). Transfer curves of UHV-Ni contacted ML MoS₂ FETs with $L_{\rm CH} \sim 85$ nm before and after various annealing process steps. e). $I_{\rm on}$ of UHV-Ni contacted ML MoS₂ FETs at $V_{\rm GS} = 1.5$ V before and after annealing at different temperatures. f). Contact resistance of UHV-Ni contacted MoS₂ FETs at $n \sim 0.9 \times 10^{13}$ cm⁻² before and after annealing at different temperatures.

When identifying the desired metal contact to TMD channels, thermal stability considerations are of utmost relevance as well, since the metal-to-channel interface will likely be exposed to various annealing conditions during the back-end of line (BEOL) chip processing. To evaluate the thermal reliability of Bi and Ni metal contacts, we compared the electrical characteristics of Bi

and Ni contacted ML MoS₂ FETs after annealing at different temperatures. Moreover, we also performed XPS and TEM experiments to analyze the interface properties before and after UHV annealing.

Annealing is performed in a high vacuum chamber at 10^{-8} Torr. Annealing involves 1-hour exposure of a given sample to an elevated temperature, followed by electrical characterization. The same sample is then exposed to an even higher temperature and then measured again etc. For Bi-contacted devices, annealing at temperatures from 100° C to 400° C in increments of 100° C has been carried out. Figure 3a) presents the transfer curves of HV-Bi contacted ML MoS₂ FETs before and after 400° C annealing. Interestingly, and different from prior publications²², no degradation of both, the on-state and off-state performance is observed. The distribution of I_{on} -and R_c -values are shown in Figure 3b) and c). Very similar current and contact resistance values after different annealing conditions indicate a good thermal reliability of our Bi contacts to MoS₂. Our experimental results are significantly different from previously reported outcomes, which observed a significant contact resistance degradation after annealing at only 200° C²². The explanation lies in the capping layer of Au that was subsequently deposited on top of Bi during the same deposition, as well as the fact that our annealing was performed in a high vacuum chamber, which prevents oxidation of Bi during the annealing process.

Other performance metrics of Bi contacted devices after annealing at different temperatures are shown in Supplementary Figure S6. The transconductance and mobility remain almost unchanged, which is indication of good thermal reliability of the channel material and metal-to-TMD contact interfaces up to 400°C. The inverse subthreshold slope shows a degraded behavior after annealing at 200°C, which occurs simultaneously with a negative threshold voltage shift. As will be discussed in greater detail below in the context of Figure 4e), annealing at elevated

temperatures results in diffusion of Bi and a reduced source-to-drain channel length, which is likely the cause of the observed changes in SS and V_{th} , consistent with a stronger electrostatic control of the channel potential by the source/drain metal contacts as discussed by us previously.⁴

The thermal reliability of Ni contacted ML MoS $_2$ is shown in Figure 3d). After 100°C annealing, the on-current is substantially degraded compared with pristine devices. The average I_{on} current degrades from 200 μ A/ μ m to 125 μ A/ μ m as shown in Figure 3e), while the average contact resistance increases from 2000 ohm· μ m to 3000 ohm· μ m. Figure S7 shows key performance metrics of Ni contacted devices before and after annealing, including transconductance, mobility, inverse subthreshold slope and threshold voltage. After 100°C annealing, the average transconductance is slightly reduced if compared to pristine devices, consistent with the observed trend in on- current I_{on} and contact resistance. The mobility remains unchanged, similar to the Bicontacted devices, indicating that the channel quality has not been affected by the annealing procedure. As apparent from Supplementary Figure S7, we do not observe a change in the inverse threshold slope or threshold voltage up to the rather moderate annealing condition of 100°C, which could not be increased due to dielectric breakdown that occurred at 200°C annealing.

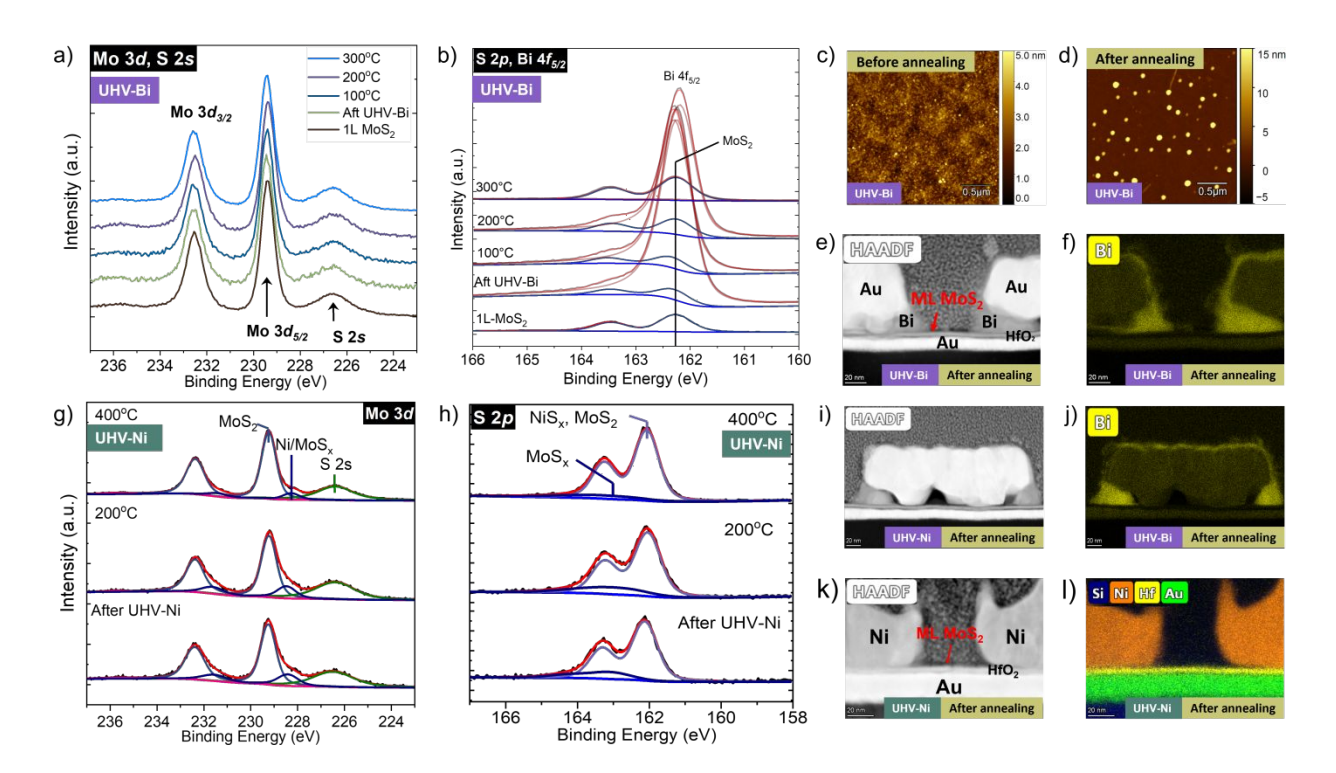


Figure 4. Interface study of Ni/MoS₂ and Bi/MoS₂ after annealing process. XPS spectra for a) Mo 3d, and b) Bi 4f and S 2p core levels of MoS₂ samples before and after annealing at 100°C, 200°C and 300°C. c) and d) AFM image of Bi/MoS₂ sample before and after 300°C annealing. e) Cross-section STEM and f) Bi elemental mapping image of Bi/Au contacted ML MoS₂ FETs with L_{ch} = 45nm after 400°C annealing. i) Cross-section STEM and j) Bi element mapping image of a second Bi/Au contact bar after 400°C annealing process. XPS spectra for (g) Mo 3d and (h) S 2p core levels of Ni/MoS₂ interface before and after annealing at 200°C and 400°C. k) Cross-section STEM and j) Si/Ni/Hf/Au elemental mapping image of Ni contacted ML MoS₂ FETs with L_{ch} = 45nm after 200°C annealing.

After metal deposition under UHV conditions, the samples were annealed following the approach described above, where XPS measurements were taken after annealing the sample for one hour e.g. at 100 °C and then subsequently increasing the temperature in increments of 100 °C. An

apparent metallic feature in Bi 4f is observed up to 200 °C, but the intensity significantly decreases after 300 °C annealing as shown in Figure 4b). This is because the vapor pressure of Bi becomes larger than ~6×10⁻⁹ mbar at 300 °C, which is sufficient to evaporate Bi in a few minutes.^{39,40} However, Bi clusters are still visible on the MoS₂ surface after an hour of annealing at 300 °C as shown in Figure 4d). All possible interfacial reaction products, such as Bi₂S₃, MoBi_xS_v, MoS_x, and BiC, are below the detection limit of XPS before and after the annealing process, as shown in Figure 4a) and 4b). AFM results in Figure 4d) show no visible damage or reaction product on the MoS₂ surface while the annealing process is up to 300°C. Figure 4e) and f) present cross-section TEM images and Bi element mapping after annealing at 400°C of an exemplary UHV-Bi contacted ML MoS₂ FET. Bi is clearly visible after this high temperature process steps at the source/drain metal corners. Figure 4i) and j) show yet another Bi/Au contact bar post anneal. As in the first example, the Bi only concentrates on two corners of the contact bar. According to the results observed in XPS, AFM, and TEM, it was confirmed by the TEM results that Bi remained at the contact interface without detectable chemical reaction with MoS₂ after the annealing process. In particular, in the Bi/Au contact, it was directly confirmed that Au capping reduced the evaporation of Bi, and Bi was intensively diffused into the surface and the corners of metal contact and MoS2 thereby playing a significant role in the electric contact behavior.

Similar to the Bi-case studied in Figure 4a) and b), we also studied the impact of temperature on the UHV-Ni contacts. Figure 4k) and l) present cross-section TEM images and Si/Ni/Hf/Au elements mapping after annealing at 200°C of an exemplary UHV-Ni contacted ML MoS₂ FET. The observation from Figure 4g) is that the FWHM of the MoS₂ feature in Mo 3d does not notably change up to 400 °C. However, after the 400 °C annealing process, it was detected that

the Ni/MoS_x feature was significantly decreased, as shown in Figure 4g). The Ni/MoS_x feature change after 200 °C annealing was close to the detection limit of XPS that decreased in the relative Ni/MoS_x intensity by about 0.1% (20.2% \rightarrow 20.1%), while the contact resistance in the actual electrical device was more sensitive because of the device performance degradation. Ni is known to form a covalent-like bonding on MoS₂, ¹⁵ and it was reported that Ni diffuses into MoS₂, degrading contact properties. ²¹ After annealing, the Ni atoms clustered to be islands, as shown in the AFM image of Figure S8, and an island located above defects because of the locally higher surface energy. In turn, the XPS intensity of the Ni/MoS_x feature can be reduced by being covered by Ni. An concomitant increase in the S 2s intensity is also consistent with further thermally activated S out diffusion, similar to the discussion above for Figure 2.

Conclusions

In this study, the impact of interface reaction/chemistry on the electrical performance of ML MoS_2 FETs is investigated. Ultrahigh vacuum deposited Ni contacts significantly reduce the contact resistance to ML MoS_2 FETs compared with Ni contacts deposited under high vacuum conditions. XPS results reveal that the Ni/ MoS_x feature in the UHV-Ni sample is noticeably observed in the intensity and the binding energy compared to HV Ni sample. This is likely due to the reduction of competitive reactions with residual gas species (e.g. OH, H_2O) during UHV deposition which otherwise result in oxidation reactions under HV. The thermal stability study of Ni contact shows the contact resistance degradation as well as a decrease in the bonding species of Ni/ MoS_x in the in-situ XPS investigation during the annealing process. Different from Ni contacts, the contact resistance of Bi contacted ML MoS_2 FETs shows no dependence on the deposition environment, since it is mainly a result of the vdW gap present in the contact region. Regardless of the vacuum conditions, we did not detect a chemical reaction between Bi and

 MoS_2 . The thermal stability study of the Bi/Au contact shows no significant contact resistance degradation after the annealing process, while the $Bi-MoS_2$ chemical reaction products remain below the detection limit of XPS.

Methods

CVD ML MoS₂ FETs fabrication and measurement

CVD ML MoS₂ triangles on SiO₂/Si substrate are purchased from 2D Semiconductors. ML MoS₂ single crystals are wet transferred on to the local bottom gate substrates. The local bottom gate substrates consist of a stack of Cr/Au(2/13nm) as gate metal, 2.8nm and 5.5nm HfO₂ as dielectric layer grown by ALD. After the wet transfer process, the sample is annealed at a pressure of ~5×10⁻⁸ torr at 200°C for 2 hours. Optical microscopy is used to identify flakes located on local bottom gates and the sample is spin coated with photoresist PMMA and baked at 180°C for 5mins. Next, source/drain contacts are patterned by a JEOL JBX-8100FS E-Beam Writer system and developed in a IPA/DI solution followed by e-beam evaporation of 20nm Bi and 50nm Au as contact metal under HV or UHV vacuum conditions. Alternatively, 70nm Ni is deposited under HV or UHV conditions as described in the main text. Next, the sample undergoes a lift-off process. After the device fabrication, the electrical characterization is performed in a Lake Shore CPX-VF probe station using an Agilent 4155C Semiconductor Parameter Analyzer at room temperature in high vacuum (10⁻⁶ Torr). Standard DC sweeps are used in the electrical measurements for all devices. All devices are measured as fabricated.

Monochromatic XPS characterization of CVD ML MoS2 and sample preparation

CVD ML MoS₂ on SiO₂/Si substrate were purchased from 2Dlayer. For XPS characterization, a monochromatic Al Kα X-ray source emitting at 1486.7 eV energy and an Omicron EA125 hemispherical analyzer were utilized.²⁷ To ensure precise calibration of the EA125 energy analyzer, standard ASTM procedures were followed.⁴¹ This calibration process involved affixing sputter-cleaned Au, Ag, and Cu foils to the manipulator for convenient calibration. XPS core level scans

were conducted pre- and post-deposition of metal contacts (Ni and Bi), employing a take-off angle of 45° and a resolution of 0.05 eV. The AAnalyzer peak fitting software facilitated the analysis of all acquired features, ensuring meticulous spectral fitting.^{29,40} Throughout this process, uniformity was meticulously maintained across all spectra parameters for each feature. This encompassed the background function, peak shape, and peak width, thereby enhancing the accuracy of the analysis.

Thermal annealing of ML MoS₂ FETs and electrical characterization

After the electrical characterization of MoS_2 FETs, the same sample is annealed at a pressure of $\sim 5 \times 10^{-8}$ torr at each temperature for 1 hour, 100/200/300/400 °C. After every annealing step, the same sample is electrically characterized in a high vacuum probe station.

Transmission Electron Microscopy characterization of ML MoS₂ FETs

High-resolution scanning transmission electron microscope (STEM) were conducted on a Thermo Fisher Scientific TALOS 200X operated at 200 kV. For the TEM samples, fabrication was done using a Thermo Fisher Helios 4G Dual Beam SEM/FIB To protect the sample from ion beam damage, a thin Pt protection layer was deposited on the top surface. The lamella was then carefully thinned to ~100 nm using ion milling under low voltage (2 keV). Chemical composition analysis was carried out using energy-dispersive X-ray spectroscopy (EDS) mode in the STEM.

Supporting Information

Additional details on total resistance versus channel length for contact resistance extraction, sheet resistance versus carrier density, output characteristics, inverse subthreshold slope and threshold voltage, performance metrics of Bi/Ni contacted devices at different annealing temperatures, XPS spectra for Ni element after different annealing temperatures.

Author information

Corresponding Author

*sun996@purdue.edu

Author contributions

Z. S., S.Y.K. and X.W. designed the experiments and fabricated the devices. S.Y.K. performed the XPS experiments. S.Y.K., X.W. and R.M.W. analyzed the XPS results, Z. S. and J. C. discussed and analyzed the data and results. H.Y.L. performed the numerical calculation, Z. S. and Y. T. conducted the electrical characterization. J. S. and H. W. performed the TEM characterization. C.S. performed FIB lift-out for TEM specimens. Z. S., S.Y. K., R. M. W., Z. C. and J. A. wrote the manuscript.

Notes

The authors declare no competing interests.

Acknowledgements

This work is in part supported by Intel Corporation.

J. S., C.S. and H.W. acknowledge the support from the U.S. Office of Naval Research (ONR, N00014-20-1-2600) and the U.S. National Science Foundation (DMR-2016453) for the SEM/FIB and STEM/EDS work. S.Y.K., X.W. and R.M.W. acknowledges the support in part for the film synthesis and surface analysis by NEWLIMITS, a center in nCORE, a Semiconductor Research Corporation (SRC) program sponsored by NIST through award number 70NANB17H041, and by the National Science Foundation through award DMR-2002741.

We thank Professor Xinghang Zhang for providing suggestions for the FIB lift-out.

References

- (1) Chung, Y.-Y.; Yun, W.-S.; Chou, B.-J.; Hsu, C.-F.; Yu, S.-M.; Arutchelvan, G.; Li, M.-Y.; Lee, T.-E.; Lin, B.-J.; Li, C.-Y.; Wei, A.; Sathaiya, D. M.; Chung, C.-T.; Liew, S.-L.; Hou, V. D.-H.; Chang, W.-H.; Liu, B.-H.; Chen, C.-W.; Su, C.-Y.; Kei, C.-C.; Cai, J.; Wu, C.-C.; Wu, J.; Lee, T.-Y.; Chien, C.-H.; Cheng, C.-C.; Radu, I. P. Monolayer-MoS2 Stacked Nanosheet Channel with C-Type Metal Contact. In *2023 International Electron Devices Meeting (IEDM)*; 2023; pp 1–4. https://doi.org/10.1109/IEDM45741.2023.10413837.
- (2) Dorow, C. J.; Schram, T.; Smets, Q.; O'Brien, K. P.; Maxey, K.; Lin, C.-C.; Panarella, L.; Kaczer, B.; Arefin, N.; Roy, A.; Jordan, R.; Oni, A.; Penumatcha, A.; Naylor, C. H.; Kavrik, M.; Cott, D.; Graven, B.; Afanasiev, V.; Morin, P.; Asselberghs, I.; Lockhart de La Rosa, C. J.; Sankar Kar, G.; Metz, M.; Avci, U. Exploring Manufacturability of Novel 2D Channel Materials: 300 Mm Wafer-Scale 2D NMOS & PMOS Using MoS2, WS2, & WSe2. In *2023 International Electron Devices Meeting (IEDM)*; 2023; pp 1–4. https://doi.org/10.1109/IEDM45741.2023.10413874.
- (3) Chou, A.-S.; Hsu, C.-H.; Lin, Y.-T.; Arutchelvan, G.; Chen, E.; Hung, T. Y. T.; Hsu, C.-F.; Chou, S.-A.; Lee, T.-E.; Madia, O.; Doornbos, G.; Su, Y.-C.; Azizi, A.; Sathaiya, D. M.; Cai, J.; Wang, J.-F.; Chung, Y.-Y.; Wu, W.-C.; Neilson, K.; Yun, W.-S.; Hsu, Y.-W.; Hsu, M.-C.; Hou, F.-R.; Shen, Y.-Y.; Chien, C.-H.; Wu, C.-C.; Wu, J.; Wong, H.-S. P.; Chang, W.-H.; van Dal, M.; Cheng, C.-C.; Wu, C.-I.; Radu, I. P. Status and Performance of Integration Modules Toward Scaled CMOS with Transition Metal Dichalcogenide Channel. In *2023 International Electron Devices Meeting (IEDM)*; 2023; pp 1–4. https://doi.org/10.1109/IEDM45741.2023.10413779.
- (4) Sun, Z.; Pang, C.-S.; Wu, P.; Hung, T. Y. T.; Li, M.-Y.; Liew, S. L.; Cheng, C.-C.; Wang, H.; Wong, H.-S. P.; Li, L.-J.; Radu, I.; Chen, Z.; Appenzeller, J. Statistical Assessment of High-Performance Scaled Double-Gate Transistors from Monolayer WS2. *ACS Nano* **2022**, *16* (9), 14942–14950. https://doi.org/10.1021/acsnano.2c05902.
- (5) Das, S.; Chen, H.-Y.; Penumatcha, A. V.; Appenzeller, J. High Performance Multilayer MoS ₂ Transistors with Scandium Contacts. *Nano Lett.* **2013**, *13* (1), 100–105. https://doi.org/10.1021/nl303583v.
- (6) English, C. D.; Shine, G.; Dorgan, V. E.; Saraswat, K. C.; Pop, E. Improved Contacts to MoS2 Transistors by Ultra-High Vacuum Metal Deposition. *Nano Lett.* **2016**, *16* (6), 3824–3830. https://doi.org/10.1021/acs.nanolett.6b01309.
- (7) Cao, Z.; Lin, F.; Gong, G.; Chen, H.; Martin, J. Low Schottky Barrier Contacts to 2H-MoS2 by Sn Electrodes. *Appl. Phys. Lett.* **2020**, *116* (2), 022101. https://doi.org/10.1063/1.5094890.
- (8) Li, W.; Gong, X.; Yu, Z.; Ma, L.; Sun, W.; Gao, S.; Köroğlu, Ç.; Wang, W.; Liu, L.; Li, T.; Ning, H.; Fan, D.; Xu, Y.; Tu, X.; Xu, T.; Sun, L.; Wang, W.; Lu, J.; Ni, Z.; Li, J.; Duan, X.; Wang, P.; Nie, Y.; Qiu, H.; Shi, Y.; Pop, E.; Wang, J.; Wang, X. Approaching the Quantum

- Limit in Two-Dimensional Semiconductor Contacts. *Nature* **2023**, *613* (7943), 274–279. https://doi.org/10.1038/s41586-022-05431-4.
- (9) Jiang, J.; Xu, L.; Du, L.; Li, L.; Zhang, G.; Qiu, C.; Peng, L.-M. Yttrium-Doping-Induced Metallization of Molybdenum Disulfide for Ohmic Contacts in Two-Dimensional Transistors. *Nat. Electron.* **2024**, 1–12. https://doi.org/10.1038/s41928-024-01176-2.
- (10) Liu, M.; Wei, S.; Shahi, S.; Jaiswal, H. N.; Paletti, P.; Fathipour, S.; Remškar, M.; Jiao, J.; Hwang, W.; Yao, F.; Li, H. Enhanced Carrier Transport by Transition Metal Doping in WS2 Field Effect Transistors. *Nanoscale* **2020**, *12* (33), 17253–17264. https://doi.org/10.1039/D0NR01573C.
- (11) Liu, H.; Fang, L.; Zhu, X.; Zhu, C.; Sun, X.; Xu, G.; Zheng, B.; Liu, Y.; Luo, Z.; Wang, H.; Yao, C.; Li, D.; Pan, A. Epitaxial van Der Waals Contacts for Low Schottky Barrier MoS2 Field Effect Transistors. *Nano Res.* **2023**, *16* (9), 11832–11838. https://doi.org/10.1007/s12274-022-5229-y.
- (12) Smyth, C. M.; Addou, R.; McDonnell, S.; Hinkle, C. L.; Wallace, R. M. Contact Metal–MoS ₂ Interfacial Reactions and Potential Implications on MoS ₂ -Based Device Performance. *J. Phys. Chem. C* **2016**, *120* (27), 14719–14729. https://doi.org/10.1021/acs.jpcc.6b04473.
- (13) McDonnell, S.; Smyth, C.; Hinkle, C. L.; Wallace, R. M. MoS₂ –Titanium Contact Interface Reactions. *ACS Appl. Mater. Interfaces* **2016**, *8* (12), 8289–8294. https://doi.org/10.1021/acsami.6b00275.
- (14) Dong, H.; Gong, C.; Addou, R.; McDonnell, S.; Azcatl, A.; Qin, X.; Wang, W.; Wang, W.; Hinkle, C. L.; Wallace, R. M. Schottky Barrier Height of Pd/MoS2 Contact by Large Area Photoemission Spectroscopy. *ACS Appl. Mater. Interfaces* **2017**, *9* (44), 38977–38983. https://doi.org/10.1021/acsami.7b10974.
- (15) Wang, X.; Kim, S. Y.; Wallace, R. M. Interface Chemistry and Band Alignment Study of Ni and Ag Contacts on MoS ₂. *ACS Appl. Mater. Interfaces* **2021**, *13* (13), 15802–15810. https://doi.org/10.1021/acsami.0c22476.
- (16) Smyth, C. M.; Addou, R.; McDonnell, S.; Hinkle, C. L.; Wallace, R. M. WSe2-Contact Metal Interface Chemistry and Band Alignment under High Vacuum and Ultra High Vacuum Deposition Conditions. *2D Mater.* **2017**, *4* (2), 025084. https://doi.org/10.1088/2053-1583/aa6bea.
- (17) Smyth, C. M.; Addou, R.; Hinkle, C. L.; Wallace, R. M. Origins of Fermi-Level Pinning between Molybdenum Dichalcogenides (MoSe ₂, MoTe ₂) and Bulk Metal Contacts: Interface Chemistry and Band Alignment. *J. Phys. Chem. C* **2019**, *123* (39), 23919–23930. https://doi.org/10.1021/acs.jpcc.9b04355.
- (18) Smyth, C. M.; Walsh, L. A.; Bolshakov, P.; Catalano, M.; Addou, R.; Wang, L.; Kim, J.; Kim, M. J.; Young, C. D.; Hinkle, C. L.; Wallace, R. M. Engineering the Palladium–WSe2 Interface Chemistry for Field Effect Transistors with High-Performance Hole Contacts. *ACS Appl. Nano Mater.* **2019**, *2* (1), 75–88. https://doi.org/10.1021/acsanm.8b01708.

- (19) Shen, P.-C.; Su, C.; Lin, Y.; Chou, A.-S.; Cheng, C.-C.; Park, J.-H.; Chiu, M.-H.; Lu, A.-Y.; Tang, H.-L.; Tavakoli, M. M.; Pitner, G.; Ji, X.; Cai, Z.; Mao, N.; Wang, J.; Tung, V.; Li, J.; Bokor, J.; Zettl, A.; Wu, C.-I.; Palacios, T.; Li, L.-J.; Kong, J. Ultralow Contact Resistance between Semimetal and Monolayer Semiconductors. *Nature* **2021**, *593* (7858), 211–217. https://doi.org/10.1038/s41586-021-03472-9.
- (20) Wang, Y.; Kim, J. C.; Wu, R. J.; Martinez, J.; Song, X.; Yang, J.; Zhao, F.; Mkhoyan, A.; Jeong, H. Y.; Chhowalla, M. Van Der Waals Contacts between Three-Dimensional Metals and Two-Dimensional Semiconductors. *Nature* **2019**, *568* (7750), 70–74. https://doi.org/10.1038/s41586-019-1052-3.
- (21) Walter, T. N.; Cooley, K. A.; Domask, A. C.; Mohney, S. E. Nickel Diffusion into MoS2 and the Effect of Annealing on Contact Resistance. *Mater. Sci. Semicond. Process.* **2020**, *107*, 104850. https://doi.org/10.1016/j.mssp.2019.104850.
- (22) Chou, A.-S.; Wu, T.; Cheng, C.-C.; Zhan, S.-S.; Ni, I.-C.; Wang, S.-Y.; Chang, Y.-C.; Liew, S.-L.; Chen, E.; Chang, W.-H.; Wu, C.-I.; Cai, J.; Wong, H.-S. P.; Wang, H. Antimony Semimetal Contact with Enhanced Thermal Stability for High Performance 2D Electronics. In *2021 IEEE International Electron Devices Meeting (IEDM)*; IEEE: San Francisco, CA, USA, 2021; p 7.2.1-7.2.4. https://doi.org/10.1109/IEDM19574.2021.9720608.
- (23) Smithe, K. K. H.; English, C. D.; Suryavanshi, S. V.; Pop, E. Intrinsic Electrical Transport and Performance Projections of Synthetic Monolayer MoS ₂ Devices. *2D Mater.* **2016**, *4* (1), 011009. https://doi.org/10.1088/2053-1583/4/1/011009.
- (24) Smithe, K. K. H.; Suryavanshi, S. V.; Muñoz Rojo, M.; Tedjarati, A. D.; Pop, E. Low Variability in Synthetic Monolayer MoS2 Devices. *ACS Nano* **2017**, *11* (8), 8456–8463. https://doi.org/10.1021/acsnano.7b04100.
- (25) Kumar, A.; Schauble, K.; Neilson, K. M.; Tang, A.; Ramesh, P.; Wong, H.-S. P.; Pop, E.; Saraswat, K. Sub-200 Ω·μm Alloyed Contacts to Synthetic Monolayer MoS2. In *2021 IEEE International Electron Devices Meeting (IEDM)*; 2021; p 7.3.1-7.3.4. https://doi.org/10.1109/IEDM19574.2021.9720609.
- (26) Wu, W.-C.; Hung, T. Y. T.; Sathaiya, D. M.; Arutchelvan, G.; Hsu, C.-F.; Su, S.-K.; Chou, A. S.; Chen, E.; Shen, Y.-Y.; Liew, S. L.; Hou, V.; Lee, T. Y.; Cai, J.; Wu, C.-C.; Wu, J.; Wong, H.-S. P.; Cheng, C.-C.; Chang, W.-H.; Radu, I. P.; Chien, C.-H. Comprehensive Study of Contact Length Scaling Down to 12 Nm With Monolayer MoS ₂ Channel Transistors. *IEEE Trans. Electron Devices* **2023**, *70* (12), 6680–6686. https://doi.org/10.1109/TED.2023.3330461.
- (27) Transition Metal Dichalcogenide Schottky Barrier Transistors: A Device Analysis and Material Comparison. In *2D Materials for Nanoelectronics*; Houssa, M., Dimoulas, A., Molle, A., Eds.; CRC Press, 2016.
- (28) Sun, Z.; Chen, C.; Robinson, J. A.; Chen, Z.; Appenzeller, J. A Mobility Study of Monolayer MoS2 on Low-κ/High-κ Dielectrics. In *2023 Device Research Conference (DRC)*; 2023; pp 1–2. https://doi.org/10.1109/DRC58590.2023.10258241.

- (29) Penumatcha, A. V.; Salazar, R. B.; Appenzeller, J. Analysing Black Phosphorus Transistors Using an Analytic Schottky Barrier MOSFET Model. *Nat. Commun.* **2015**, *6* (1), 8948. https://doi.org/10.1038/ncomms9948.
- (30) Zhou, R.; Appenzeller, J. About the Interplay between Contact and Channel Resistance in MoS2 and Its Impact on Mobility Extraction. In *2019 Device Research Conference (DRC)*; 2019; pp 135–136. https://doi.org/10.1109/DRC46940.2019.9046444.
- (31) Somvanshi, D.; Kallatt, S.; Venkatesh, C.; Nair, S.; Gupta, G.; Anthony, J. K.; Karmakar, D.; Majumdar, K. Nature of Carrier Injection in Metal/2D-Semiconductor Interface and Its Implications for the Limits of Contact Resistance. *Phys. Rev. B* **2017**, *96* (20), 205423. https://doi.org/10.1103/PhysRevB.96.205423.
- (32) Chou, A.-S.; Cheng, C.-C.; Liew, S.-L.; Ho, P.-H.; Wang, S.-Y.; Chang, Y.-C.; Chang, C.-K.; Su, Y.-C.; Huang, Z.-D.; Fu, F.-Y.; Hsu, C.-F.; Chung, Y.-Y.; Chang, W.-H.; Li, L.-J.; Wu, C.-I. High On-State Current in Chemical Vapor Deposited Monolayer MoS2 nFETs With Sn Ohmic Contacts. *IEEE Electron Device Lett.* **2021**, *42* (2), 272–275. https://doi.org/10.1109/LED.2020.3048371.
- (33) Freedy, K. M.; Zhang, H.; Litwin, P. M.; Bendersky, L. A.; Davydov, A. V.; McDonnell, S. Thermal Stability of Titanium Contacts to MoS2. *ACS Appl. Mater. Interfaces* **2019**, *11* (38), 35389–35393. https://doi.org/10.1021/acsami.9b08829.
- (34) Blair, J. C.; Ghate, P. B. Effect of Vacuum Ambience on Al–Si Contacts. *J. Vac. Sci. Technol.* **1977**, *14* (1), 79–84. https://doi.org/10.1116/1.569178.
- (35) Wallace, R. M. In-Situ Studies on 2D Materials. *ECS Trans.* **2014**, *64* (9), 109–116. https://doi.org/10.1149/06409.0109ecst.
- (36) XPS OASIS. https://xpsoasis.org/ (accessed 2024-04-22).
- (37) Gambino, J. P.; Colgan, E. G. Silicides and Ohmic Contacts. *Mater. Chem. Phys.* **1998**, *52* (2), 99–146. https://doi.org/10.1016/S0254-0584(98)80014-X.
- (38) Hieber, K.; Lassak, L. Structural and Electrical Properties of Chromium and Nickel Films Evaporated in the Presence of Oxygen. *Thin Solid Films* **1974**, *20* (1), 63–73. https://doi.org/10.1016/0040-6090(74)90034-0.
- (39) Schweppe, J.; Deslattes, R. D.; Mooney, T.; Powell, C. J. Accurate Measurement of Mg and Al K α 1,2 X-Ray Energy Profiles. *J. Electron Spectrosc. Relat. Phenom.* **1994**, *67* (3), 463–478. https://doi.org/10.1016/0368-2048(93)02059-U.
- (40) Standard Practice for Calibration of the Electron Binding-Energy Scale of an X-Ray Photoelectron Spectrometer. https://www.astm.org/e2108-16.html (accessed 2024-02-24).
- (41) Herrera-Gómez, A.; Hegedus, A.; Meissner, P. L. Chemical Depth Profile of Ultrathin Nitrided SiO2 Films. *Appl. Phys. Lett.* **2002**, *81* (6), 1014–1016. https://doi.org/10.1063/1.1494121.